Solar water splitting exceeding 10 % efficiency via low-cost Sb_2Se_3 photocathodes coupled with semitransparent perovskite photovoltaics

Received 00th January 20xx,
Accepted 00th January 20xx

Wooseok Yang[‡a,b], Jaemin Park[‡a], Hyeok-Chan Kwon[‡a], Oliver S. Hutter[c], Laurie J. Phillips[d], Jeiwan Tan[a], Hyungsoo Lee[a], Junwoo Lee[a], S. David Tilley[b], Jonathan D. Major[d] and Jooho Moon[a*]

Solar water splitting directly converts solar energy into H_2 fuel that is suitable for storage and transport. To achieve a high solar-to-hydrogen (STH) conversion efficiency, elaborate strategies yielding a high photocurrent in a tandem configuration along with sufficient photovoltage should be developed. We demonstrated highly efficient solar water splitting devices based on emerging low-cost Sb_2Se_3 photocathodes coupled with semitransparent perovskite photovoltaics. A state-of-the-art Sb_2Se_3 photocathode exhibiting efficient long-wavelength photon harvesting enabled by judicious selection of junction layers was employed as a bottom absorber component. The top semitransparent photovoltaic cells, i.e., parallelized nanopillar perovskites using an anodized aluminum oxide scaffold, allowed the transmittance, photocurrent, and photovoltage to be precisely adjusted by changing the filling level of the perovskite layer in the scaffold. The optimum tandem device, in which similar current values were allocated to the top and bottom cells, achieved an STH conversion efficiency exceeding 10% by efficiently utilizing a broad range of photons at wavelength over 1000 nm.

Introduction

Solar energy can be stored with battery technology by converting it into electricity via photovoltaic (PV) cells; however, producing H_2 fuel via photoelectrochemical (PEC) water splitting is a more efficient solution for long-term storage. The solar-to-hydrogen (STH) conversion efficiency (η_{STH}) is proportional to the device photocurrent when a sufficient photovoltage that exceeds the sum of the thermodynamic voltage for overall water splitting (1.23 V) and the overpotentials for the oxygen evolution reaction (OER) and hydrogen evolution reaction (HER) is provided. Therefore, to achieve high η_{STH}, elaborate strategies should be developed to maximize the photocurrent while producing a photovoltage suitable to drive the water-splitting reaction[1]. A dual-absorber tandem cell is a promising configuration for achieving both high photovoltage and photocurrent, allowing a theoretical maximum η_{STH} of >25%[2], but most of the η_{STH} values for PEC tandem devices consisting of OER and HER photoelectrodes have been <3%[3]. The low efficiencies of real PEC tandem devices result from the difficulties in finding an ideal combination of materials having suitable bandgaps (E_g) and band positions.

Compared with the photoanode–photocathode tandem configuration, the PV-PEC tandem configuration is advantageous as an additional voltage can be supplied by technologically mature PV cells, having no direct relationship with the water redox potentials, thereby enhancing the flexibility of the choice of materials. In this regard, higher η_{STH} values have been reported for PV-PEC tandem devices, such as $BiVO_4$ coupled with Si (η_{STH} = 7.7%)[4], III-Vs (8.1%)[5], and perovskite PVs (4.3%)[6]. However, as the device current is limited by the lower-current cell in this series-connected architecture, the η_{STH} of the high E_g (~2.4 eV) $BiVO_4$-based tandem theoretically cannot reach 10%, which is generally the target for commercialization of cost-effective systems[7]. Additionally, Luo et al.[8] used a low-E_g semiconductor $CuIn_xGa_{1-x}Se_2$ (CIGS, $E_g \approx 1.1$ eV) as a bottom electrode for a PV-PEC tandem cell in conjunction with two different perovskite PVs: $CH_3NH_3PbI_3$ ($MAPbI_3$) and $CH_3NH_3PbBr_3$ ($MAPbBr_3$). Despite the high-quality CIGS thin films, the η_{STH} values of the PV-PEC tandem devices were low—2.6% (with $MAPbI_3$ PVs) and 6.3% (with $MAPbBr_3$ PVs)—because of the non-ideal matching between the top and bottom cells. Precisely balancing the light absorption between the top and bottom electrodes as well as between the photocurrent and photovoltage thus remains a challenge for achieving a PV-PEC tandem device with a high η_{STH}. Although STH over 9% was reported by CIGS photocathodes coupled with perovskite solar cells[9], the device is not in a tandem configuration (electrically in series, but optically in parallel).

Herein, we report highly efficient PV-PEC tandem devices based on Sb_2Se_3 photocathode and semitransparent perovskite PVs. Sb_2Se_3 is an emerging low-cost photocathode material capable of harvesting solar photons with wavelengths up to 1050 nm owing to its low E_g (~1.18 eV). Despite the rapid

[a.] *Department of Materials Science and Engineering, Yonsei University, 50 Yonsei-ro Seodaemun-gu, Seoul 03722, Republic of Korea, E–mail: jmoon@yonsei.ac.kr*
[b.] *Department of Chemistry, University of Zurich, Zurich 8057, Switzerland.*
[c.] *Department of Mathematics, Physics and Electrical Engineering, Northumbria University, Newcastle upon Tyne, UK.*
[d.] *Stephenson Institute for Renewable Energy, Physics Department, University of Liverpool, Liverpool L69 7ZF, UK*

† Electronic Supplementary Information (ESI) available: Single PV-cell-PEC tandem device, light-absorption coefficient of $MAPbI_3$, faradaic efficiencies of the Sb_2Se_3 photocathodes, performances of semitransparent perovskite PVs, long-term stability test of the optimized PV-PEC tandem cell. See DOI: 10.1039/x0xx00000x

‡These authors contributed equally.

advancement of this material in the field of PEC water splitting[10–16], there is only one report of unbiased water splitting via an Sb_2Se_3 photocathode, wherein the η_{STH} was low (1.5%)[3]. The state-of-the-art Sb_2Se_3 photocathode was fabricated by employing appropriate junction layers, which significantly enhanced the performance, particularly the long-wavelength photon-harvesting capability. For the top perovskite PVs, we employed nanopillar-structured semitransparent PVs[17,18], which allowed us to precisely control the light absorption and performance of the top electrode, thereby helping to determine optimum transmittance and performance as a complementary top electrode for high η_{STH}. The PV-PEC tandem device exhibited a photocurrent density of 8.3 mA cm^{-2} without an external bias, corresponding to an η_{STH} exceeding 10%.

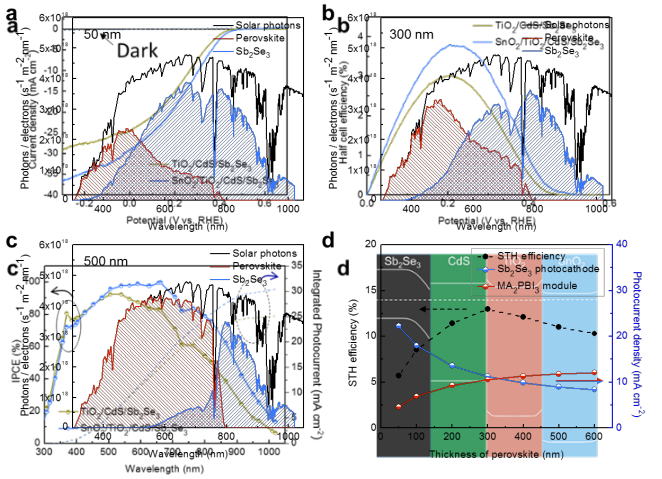

Fig. 2 Analysis of the STH efficiency of virtual top PV cells and bottom Sb_2Se_3 photocathodes depending on the thickness of the PV cells. AM 1.5G photon flux and the theoretical electron flux of the top PV cell and the bottom Sb_2Se_3 electrode when the thickness of the perovskite was **a** 50 nm, **b** 300 nm, and **c** 500 nm. **d** Calculated STH_E efficiencies and photocurrent densities of the PV cells and the photocathode.

Results and discussion

Development of Sb_2Se_3 photocathode as bottom electrode for PV-PEC tandem cell

As the bottom electrode in a tandem cell harnesses the transmitted photons through the top electrode (i.e., the unabsorbed photons within the absorption range and the photons whose wavelengths are longer than the absorption edges of the top semiconductors), a high quantum efficiency is required in the long-wavelength region on the bottom electrode for an efficient tandem cell. Thus, efficient separation of the generated charges must be achieved to avoid undesirable recombination of the long-wavelength photons. Adjusting the band alignment in a photocathode by adopting proper junction layers is a well-known technique for reducing recombination and thereby enhancing the photocurrent density. Thus far, the best-performing Sb_2Se_3 photocathode with regard to the half-cell efficiency, representing the efficiency of the half-cell reaction with respect to its thermodynamic potential, was part of a Pt/TiO_2/CdS/Sb_2Se_3/Au/FTO configuration[3]. In this study, we deposited a thin SnO_2 layer on the TiO_2 layer to facilitate the separation of the photoexcited charges. The structure and composition characterization of the laminated SnO_2/TiO_2/CdS/Sb_2Se_3 junction show distinct interfaces of the constituent layers with the thicknesses of CdS, TiO_2, and SnO_2 to be 22, 40, and 30 nm, respectively (see Fig. S1-2 and Note S1 in the ESI†). In both Sb_2Se_3 photocathodes (with and without SnO_2), Pt was used as an electrocatalyst, and C_{60} was deposited between Pt and TiO_2 to enhance the stability[11] (see the Experimental section for details). As shown in Fig. 1a, the photocurrent density of the Sb_2Se_3 photocathodes at 0 V vs. a reversible hydrogen electrode (V_{RHE}) increased from 24 to 29 mA cm^{-2} upon the insertion of the SnO_2 layer. Consequently, the maximum half-cell efficiency value of the Sb_2Se_3 photocathodes reached 3.8%, which is the highest value reported thus far. Additionally, the incident photon-to-current conversion efficiency (IPCE) of the Sb_2Se_3 photocathode increased, particularly in a long-wavelength region (>600 nm), which is a promising result for the bottom electrode of a tandem cell (Fig. 1c). The integrated photocurrent densities (25.05 and 30.3 mA cm^{-2} for with/without the SnO_2 layer, respectively) are in agreement with the photocurrent at 0 V_{RHE} in the J–V curves. To be specific, for the SnO_2/TiO_2/CdS/Sb_2Se_3 photocathode, the integrated current is slightly higher (~5%) than that of the J–V curve. In general, small differences (e.g., ±10%) are acceptable because both techniques (i.e., J–V measurement under 1 sun illumination vs. IPCE measurement) have completely different conditions, such as calibration, wavelengths of photons, size of the light source, the distance between the light source and sample, etc. The slight decrease in the IPCE near ~350 nm resulted from the parasitic absorption by the SnO_2 layer, for which E_g is 3.6 eV. The enhanced performance of Sb_2Se_3 upon the deposition of SnO_2 is attributed to the proper band alignment, as shown in Fig. 1d. The band positions of each layer are obtained by ultraviolet photoelectron spectroscopy and UV-vis spectroscopy (Fig. S3-4, Note S2 in the ESI†). Upon the equilibration of the Fermi levels, the conduction bands continuously move to lower energy levels from Sb_2Se_3 to SnO_2 (Fig. 1d); thus, the photoexcited electrons can be separated efficiently. The equilibration of the Fermi levels also resulted in slight upper band bending between the TiO_2 and SnO_2 layers, which might prevent the transfer of photo-induced electrons. However, electrons in the conduction band of TiO_2 can transfer even under a significant upper band bending condition[19]. Thus, the accumulated electrons can be transferred to the SnO_2 layer while preventing the diffusion of the electrons back to the junction for recombination (see Note S3 for in-depth explanation of the tunneling current through the TiO_2/SnO_2 interface). Additionally, owing to the high E_g of SnO_2 (~3.6 eV), the separated electrons were unlikely to recombine with the holes injected in the opposite direction. The enhanced charge separation due to the electron selective contact slightly enhanced the photovoltage and improved the photocurrent

on an Au/FTO substrate. **d** Equilibrium band alignment diagram of the Sb_2Se_3/CdS/TiO_2/SnO_2 heterojunction. The dimensions are not to scale.

owing to the increased utilization of long-wavelength photons. Although SnO_2 alone was previously used as a protective layer for a Cu_2O photocathode[20], to the best of our knowledge, this is the first demonstration of SnO_2 on top of TiO_2 to enhance the charge separation and thus the photocurrent density of photocathodes for PEC water splitting. Notably, the TiO_2/CdS layer has been widely employed in various photocathodes, e.g., Sb_2Se_3[21], Cu_2S[22], Cu_2ZnSnS_4[23], $Cu_2BaSn(S,Se)_4$[24], and GeSe[25]. The similarity of the role of the TiO_2/CdS layer among all the photocathodes suggests that the SnO_2/TiO_2/CdS junction layer can be used to enhance the charge separation in various photocathodes.

Ideal PV cell exploration for Sb_2Se_3 photocathode tandems

As we obtained a promising Sb_2Se_3 photocathode capable of efficiently harvesting solar photons in a long-wavelength region, the next step was to obtain a PV cell optimized for a high η_{STH} in conjunction with the bottom electrode. As mentioned previously, an ideal top PV cell should have a high transparency and photocurrent density while producing a sufficient photovoltage. In this regard, semitransparent perovskite PV cells[17,18], which allow precise control of the transmittance and performance, are attractive top electrodes. As a single semitransparent perovskite PV cell and the Sb_2Se_3 photocathode produced photovoltages of approximately 1.0 and 0.45 V, respectively, the overall voltage developed by the tandem cell is approximately 1.45 V when the Sb_2Se_3 photocathode is connected to a single PV cell. The voltage of 1.45 V can initiate unassisted water splitting, but the efficiency is too low; thus, a significantly higher voltage is needed (Fig. S5, ESI†). In this regard, a series connection of two semitransparent PVs, which can produce a photovoltage of approximately 2 V (*vide infra*), represents a better approach. To gain insight into the efficiency of the PV-PEC tandem with the semitransparent perovskite PV and the Sb_2Se_3 photocathode, we evaluated η_{STH} with respect to the transmittance of the top PV cells.

Fig. 2a–c show the solar photon harvesting by the top perovskite cells and the bottom Sb_2Se_3 photocathode depending on the transmittance of the top cell. Regarding the light absorption of the top PV cell, the light-absorption coefficient (α) of $MAPbI_3$ experimentally determined in the literature was used (Fig. S6, ESI†)[26]. The following assumptions were made to calculate η_{STH}: there were no reflections or optical losses for the different PV components (TiO_2, the hole-transport layer, etc.), all the light absorbed by the perovskite layer contributed to the current, and all the photons transmitted through the PV cell reached the bottom Sb_2Se_3, followed by conversion into current, according to the IPCE values in Fig. 1c (SnO_2/TiO_2/CdS/Sb_2Se_3 junction). The use of the IPCE values at 0 V_{RHE} to calculate the current density of the Sb_2Se_3 photocathodes behind the PV cells was reasonable because the photovoltage produced by the PV cells (~2.0 V) was substantial (*vide infra*). Additionally, it should be noted that the current values of the two perovskite cells connected in series corresponded to half of the absorbed photons. The overall current value of the tandem cell was determined by the lower current device between the top and bottom cells and was converted into η_{STH} via multiplication by 1.23 V, which is the thermodynamic voltage for water splitting. Additionally, the faradaic efficiency was assumed to be 100% (i.e., the overall current contributed to H_2 production, without any side reactions). This assumption was valid because the faradaic efficiency of the Sb_2Se_3 photocathode was close to unity regardless of the operating current density (Fig. S7, ESI†). Here we tried to estimate the maximum achievable efficiency by coupling our Sb_2Se_3 photocathode with an 'ideal' perovskite solar cell. Although there are some deviations from actual perovskite devices, we believe this is an appropriate way to envision the maximum achievable goals, and to evaluate the level of our current system with respect to the ideal case.

As shown in Fig. 2a, when the perovskite layer was too thin (50 nm), the amount of photons harvested by the bottom cell (blue line) was significantly larger than that harvested by the top cell (red line). In this case, the overall current was limited by the top-cell current; thus, η_{STH} was approximately 5% (Fig. 2d). The photon harvesting was reduced by the thin perovskite layer at wavelengths of >500 nm because α decreased with an increase in the wavelength (Fig. S6, ESI†). For instance, quantitatively, the α of $MAPbI_3$ at 400 nm (~3×10^5 cm^{-1}) was approximately one order of magnitude higher than that at 700 nm (~3×10^4 cm^{-1}), implying that a 10 times thicker $MAPbI_3$ film was needed to fully harvest 700-nm photons compared with 400-nm photons. Therefore, when the perovskite layer was sufficiently thick (500 nm, Fig. 2c), most of the incident photons <800 nm were harvested by the top cell. However, in this case, the efficiency was limited by the poor current of the bottom cell. With the optimum thickness of the perovskite layer, some photons that were not absorbed by the top cell in the range of 500 nm < λ < 800 nm were absorbed by the bottom Sb_2Se_3 photocathode; thus, similar current values were allocated to

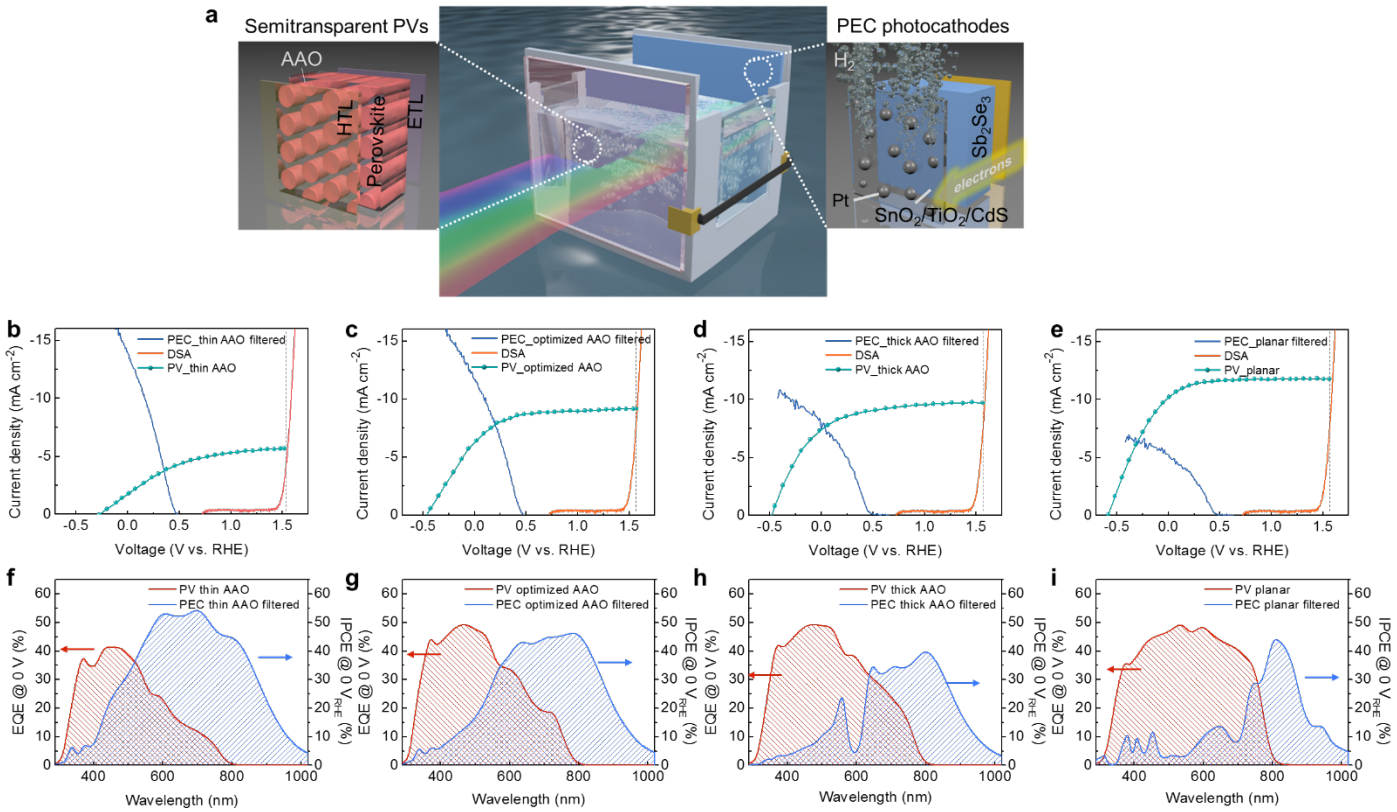

Fig. 3 Three-electrode measurements and quantum efficiencies of the top PVs and the bottom photocathodes. a Schematic of the tandem configuration. J–V curves of the semitransparent perovskite PVs, DSA, and Sb_2Se_3 photocathodes behind the PVs with **b** thin AAO, **c** optimized AAO, **d** thick AAO, and **e** a planar thin film. The Sb_2Se_3 photocathodes and DSA were immersed in an H_2SO_4 electrolyte (pH of 1), and simulated 1-sun AM 1.5G illumination was applied. IPCEs and EQEs of the photocathodes and the PVs with **f** thin AAO, **g** optimized AAO, **h** thick AAO, and **i** planar thin film.

the top and bottom cells (Fig. 2b). Consequently, the maximum photocurrent was 10.7 mA cm^{-2}, corresponding to η_{STH} = 13%. There may be deviations between this estimation and a real device, as the evaluation was performed under certain assumptions; nonetheless, the results clearly indicate that an η_{STH} exceeding 10% may be achievable in a practical device by optimizing the light-harvesting balance between the top PVs and the bottom Sb_2Se_3 photocathodes.

Despite the importance of a highly transparent and efficient PV for a high η_{STH}, fabricating a PV cell with both a high transparency and high performance is challenging[27]. The nonlinear relationship between the transmittance and performance in normal thin-film PVs, in addition to the exclusion of conventional opaque layers (e.g., Au contact in perovskite PVs), causes inevitable losses in the performance of semitransparent PVs (see Fig. S8, Note S4, and Table S1 in the ESI†). Our group previously reported a novel strategy for obtaining semitransparent perovskite PVs by utilizing an anodized aluminum oxide (AAO) template[17,18]. With parallelized perovskite nanopillar arrays embedded in the AAO template, the transmittance and performance of the PV cells were precisely controlled by adjusting the filling level of the perovskite layer in the AAO scaffold (see Fig. S9-10, Note S5, Table S2 in the ESI†). The novel strategy yielded the optimum PVs with a sufficient transparency, photocurrent, and photovoltage suitable for a high η_{STH}. Moreover, a different light scattering behaviour induced by the periodic AAO structure is another advantage of the AAO-templated perovskite cells. We measured the total and specular transmittance of the planar and AAO cells (Fig. S11a-b). The planar cell shows a large difference between total and specular transmittance, while in the AAO cell both transmittances are almost the same. This indicates that many photons transmitted through the planar perovskite film tend to scatter presumably due to the rough surface. In contrast, the uniform and highly ordered structure in the AAO cell enabled most of the transmitted photons to be specular (Fig. S11c-d). Therefore, with the AAO configuration, the photonic loss caused by the diffuse transmission can be minimized so that higher performance is achievable.

Three-electrode measurement for PEC-PV tandem cells

To predict the tandem operating point of each device, the current density–voltage (J–V) response of the PV cell was plotted with the J–V curves of the Sb_2Se_3 photocathode and a commercially available dimensionally stable anode (DSA, Ir- and Ru-coated Ti plate), which is known as an active OER catalyst in an acidic electrolyte. The size of DSA (~20 cm^2) is much larger than the active area of tandem cells (~ 0.2 cm^2), meaning that the overall HER and OER reactions are not constrained by the active area of DSA anode (Fig. S12a, EIS†). The stability of DSA under a similar condition to the actual tandem cells was also

tested. Fig. S12b shows the stable operation of DSA anode over days when a constant 10 mA cm^{-2} current density (similar to the maximum photocurrent of the tandem cells) was applied. The stability of DSA anode indicates that the stability of the tandem device is not limited by DSA. We also measured the scan-speed dependent current density of DSA as well as Sb_2Se_3 photocathodes (Fig. S13). DSA shows slightly a higher current density when scanned with the faster scan speed (50 mV s^{-1}) than the slow case (10 mV s^{-1}), especially at the lower-potential region, indicating that there is capacitive current. For the tandem cell test, the 20 mV s^{-1} scan speed was used as the difference between 20 and 10 mV s^{-1} was negligible in both DSA and Sb_2Se_3 photocathodes. The semitransparent PV cells were in front of the reactor containing the electrolyte, and the performance of the Sb_2Se_3 photocathode was measured under the light transmitted through the PV cells, as shown in Fig. 3a. The current values at the intersection of the Sb_2Se_3 and PV curves indicate the operating point of the tandem device. Clearly, with the thin AAO template, the low current in the PV cell limited the operating current (Fig. 3b), whereas the operating current in the planar PV-based tandem cell was limited by the low current level of the Sb_2Se_3 photocathode (Fig. 3e). With the optimum filling level (~220 nm), which resulted in balanced light absorption between the top and bottom electrodes, the operation current density was approximately 8 mA cm^{-2}, corresponding to $\eta_{STH} \approx 10\%$. Remarkably, for the high η_{STH}, the top semitransparent PV cells had an excellent light-management ability, yielding a high transparency, photocurrent, and photovoltage simultaneously. As mentioned previously, in the previous CIGS-perovskite tandem cell, the $MAPbI_3$ cell produced an insufficient photovoltage, whereas the $MAPbBr_3$ cell suffered from an inadequate photocurrent on the top cell, both of which resulted in poor efficiencies[8]. The excellent light-harvesting ability of the Sb_2Se_3 photocathodes was a key factor leading to the high η_{STH}. As shown in Fig. 3b–d, the Sb_2Se_3 photocathodes exhibited a high photocurrent density (saturation current density > 10 mA cm^{-2}) even behind the semitransparent PVs. In contrast, in the previous Cu_2O-perovskite tandem cell, the photocurrent density of the perovskite PV behind the Cu_2O significantly decreased; it was only ~4.6 mA cm^{-2} at the saturation points[28]. The high photocurrent density of the Sb_2Se_3 photocathode originated from the intrinsic properties of Sb_2Se_3 (low E_g of ~1.18 eV), as well as the proper interface engineering for efficient charge separation.

In addition to the operation-current evaluation, the manner in which the semitransparent PV-Sb_2Se_3 tandem utilizes photons was investigated via external quantum efficiency (EQE) and IPCE measurements, as shown in Fig. 3f-i. The measured EQE and IPCE for the top and bottom electrodes resembled the shape predicted by our theoretical analysis in Fig. 2, indicating that our estimation closely matched the real system. Similar to the theoretical prediction, the EQE values of the PV cell rapidly decreased at a wavelength of 500 nm when the absorber was too thin (Fig. 3f), owing to the decreasing light-absorption coefficient of perovskite over 500 nm (Fig. S2, ESI†). As the filling level increased, the EQE values of the PV cells increased, while

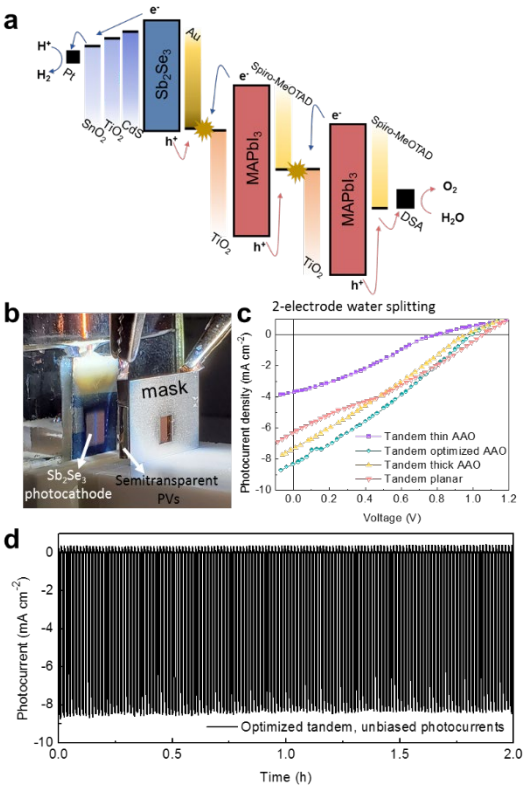

Fig. 4 Two-electrode standalone tandem device performance. **a** Energy potential diagram of the tandem device with the two PV cells and the PEC photocathode. **b** Optical photograph of the tandem device. **c** Performance of the two-electrode water-splitting tandem device with different PVs. **d** Unbiased water-splitting performance of the optimized tandem device under intermittent 1-sun illumination.

the IPCE values of the Sb_2Se_3 photocathode decreased. For the planar PV cell, the EQE graph had a symmetric shape and a sharp edge near 800 nm, while the bottom Sb_2Se_3 was able to harvest only a small portion of the photons, resulting in a low efficiency. The EQE and IPCE results were in accordance with the theoretical analysis (Fig. 2), as well as the J–V curves (Fig. 3b-e), indicating that the utilization of the photons was optimized over a broad wavelength range using our semitransparent PV-PEC tandem device.

Two-electrode unbiased water splitting by PV-PEC tandem cell

To confirm the real STH performance of the standalone PV-PEC tandem device, we performed J–V curve measurements with a two-electrode configuration, connecting the PV and Sb_2Se_3 photocathode (for H_2 evolution) with DSA (for oxygen evolution) without a reference electrode. A generalized energy diagram of the tandem device is shown in Fig. 4a; the Sb_2Se_3 photocathode was connected to two perovskite cells in series (see Fig. S14 for a schematic visualization of two perovskite PV cells connected in series), and the electrons moved to the surface of the photocathode, while the holes were transferred to the DSA. An optical photograph of the PV-PEC tandem cell is shown in Fig. 4b. The simulated light passed through the mask aperture (for defining the active area) and the semitransparent PVs and reached the bottom Sb_2Se_3 photocathode immersed in the electrolyte. The mask was sufficiently thick to block all the

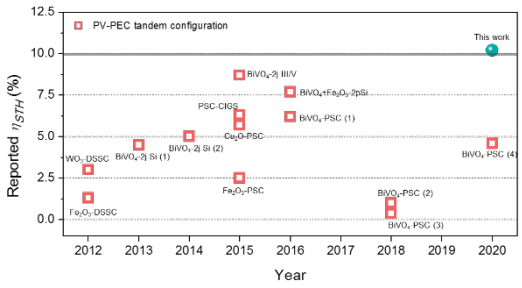

Fig. 5 η_{STH} benchmarks for the PV-PEC tandem configuration. Dye-sensitized solar cell (DSSC), PSC, 2j Si (double-junction Si solar cell), 2j III/V (double junction GaAs/InGaAsP solar cell), WO_3-DSSC and Fe_2O_3-DSSC[29], $BiVO_4$-2j Si (1)[30] and (2)[31], PSC-CIGS[8], Cu_2O-PSC[8], Fe_2O_3-PSC[32], $BiVO_4$-2j III/V[5], $BiVO_4$+Fe_2O_3-2pSi[4], and $BiVO_4$-PSC (1)[33], (2)[34], (3)[35], and (4)[36].

photons. Fig. 4c shows the J–V curves of the four different PV-PEC tandem devices with two-electrode configurations. As there are in the two-electrode configuration, the current values at 0 V represent the unbiased water-splitting rate. All these values agreed with the values predicted according to the intercept of the J–V curves for the three-electrode configuration (Fig. 3). The measured unbiased water-splitting current for the optimum tandem device was 8.3 mA cm^{-2}, corresponding to 10.2% η_{STH}. This value corresponds to approximately 78 % of the maximum achievable η_{STH} (13% η_{STH}) we estimated by assuming an ideal semi-transparent PV in Fig. 2, indicating that our AAO-based semitransparent PVs work properly as a top cell for a tandem device, even though there is some space for further improvement. The faradaic efficiency of the Sb_2Se_3 photocathode was close to 100% at a similar current (Fig. S7, ESI†). Chronoamperometry was performed under unbiased conditions with the optimum tandem device (Fig. 4d). The photocurrent under unbiased conditions remained constant for 2 h without degradation, and zero current was observed under dark conditions. The generation of H_2 bubbles by the PV-PEC tandem device under unbiased conditions is shown in Supplementary Video. The results of a long-term stability test are presented in Fig. S15 in the ESI†. The photocurrent of the tandem device under unbiased conditions remained relatively constant for 4 h, followed by a slight decline. After 10 h, the photocurrent was approximately 80% of the initial value.

Fig. 5 shows previously reported η_{STH} values for PV-PEC tandem devices. In most cases, n-type photoanodes were used, except for the two photocathode cases (perovskite solar cell (PSC)-CIGS and Cu_2O-PSC). The efficiencies of the PV photoanode devices are limited by the high E_g of the n-type semiconductors, such as WO_3 ($E_g \approx 2.7$ eV) and $BiVO_4$ ($E_g \approx 2.4$ eV), or the poor electrical properties (e.g., in the case of Fe_2O_3). The highest efficiency of η_{STH} = 8.1%, which is close to the theoretical maximum for a $BiVO_4$-based tandem cell, was obtained by connecting a double-junction GaAs/InGaAsP PV cell[5], but the III-V semiconductors are expensive, posing an obstacle for commercialization despite the high efficiency of 8.1%. The highest efficiency obtained by a photocathode-PV tandem device (PSC-CIGS)[8] was only ~6.5% owing to the lack of a strategy for achieving a proper light-harvesting balance (as discussed previously), even though an expensive PV-grade CIGS photocathode was used. Additionally, high-efficiency devices with different configurations have been recently reported, such as two series-connected Si solar cells with a dual Si photoelectrode (9.8%)[37] and PSC-CIGS (9%)[9]. However, neither of these recently reported high-efficiency devices have a tandem configuration; i.e., the cells are not placed on top of another but are placed side-by-side, resulting in parallel illumination. The tandem configuration is considered as the most promising candidate for commercial applications because of the convenient assembly and efficient solar-light utilization[38]. Therefore, our PEC-PV tandem device (with an efficiency exceeding 10%) consisting of a precisely controllable semitransparent PV cell and a low-cost Sb_2Se_3 photocathode represents an important milestone in the field of solar water splitting.

Experimental

Fabrication of Sb_2Se_3 Photocathodes

Sb_2Se_3 films were fabricated via a previously reported two-step fast-cooling close space sublimation (CSS) process[3,39]. Stoichiometric Sb_2Se_3 (Alfa Aesar, 99.999% metals basis) was used for absorber-layer growth, during which source and substrate temperatures of 365 and 320 °C, respectively, were maintained for 10 min at a pressure of 0.05 mbar. Subsequently, deposition was completed using a source temperature of 470 °C for 15 min at a pressure of 13 mbar. The films were then rapidly cooled by rolling the heater off the work tube and flowing N_2 over them at a rate of 5 L min^{-1}. Sb_2Se_3 photocathodes were completed by depositing overlayers sequentially. First, a CdS layer was deposited via chemical bath deposition (CBD). Prior to the CBD, Sb_2Se_3 samples were pre-treated in a bath containing a solution of $CdSO_4$ (Sigma–Aldrich, 99.99%) and NH_4OH (Duksan, 28 wt.%) at 60 °C for 10 min. After the pre-treatment, the CdS deposition was performed by immersing the samples in a solution containing $CdSO_4$, thiourea (99%, Sigma–Aldrich), deionized (DI) water, and NH_4OH for 5 min at 60 °C. TiO_2 and SnO_2 layers were deposited via an atomic layer deposition (ALD) process (Lucida D100, NCD Inc.). For the TiO_2 layer, tetrakis(dimethylamido)titanium (TDMAT) and H_2O were used as precursors for Ti and O, respectively. The process was performed at 120 °C, with a total of 600 ALD cycles. Each cycle comprised a TDMAT pulse of 0.3 s followed by 15 s of N_2 purging and an H_2O pulse of 0.2 s followed by 15 s of N_2 purging. The SnO_2 layer was prepared at 110 °C with tetrakis(dimethylamino)tin (TDMASn) and H_2O as the Sn and O precursors, respectively. A total of 300 ALD cycles were conducted, each comprising a TDMASn pulse of 0.3 s followed by 15 s of N_2 purging and an H_2O pulse of 0.3 s followed by 15 s of N_2 purging. The approximate growth rates of TiO_2 and SnO_2 were 0.55 and 1 Å per cycle, respectively, as estimated using an ellipsometer (alpha SE, J.A. Woollam Co. Ltd.). C_{60} was coated prior to Pt deposition to enhance the stability of the

photocathode[11]. 20 mg of C_{60} powder (99.5%, Sigma–Aldrich) was dissolved in 10 mL of chlorobenzene (99.8%, Sigma–Aldrich). The C_{60} dispersion was spin-coated twice onto the TiO_2/SnO_2-coated Sb_2Se_3 electrode at 3000 rpm for 30 s after 10 min of ultraviolet (UV) treatment. Each cycle consisted of drying at 80 °C for 2 min, and the as-dried samples were annealed for 5 min at 150 °C. Then, the Pt co-catalyst was sputtered on the samples by using an Auto Sputter Coater (Ted Pella, Redding, CA, USA) for 120 s under an applied current of 10 mA.

Fabrication of Perovskite Cells

A PSC was fabricated using a previously reported method[17,18]. A fluorine-doped tin oxide (FTO)/glass (15 Ω/square) substrate was cleaned with a detergent solution (2 vol.% of Hellmanex III in distilled water), acetone, and ethanol for 10 min each using an ultrasonic bath, followed by O_2 plasma treatment. After taping for bottom FTO electrode contact, a solution of titanium isopropoxide (0.6134 mL, 99.999%, Sigma–Aldrich) and HCl (84 µL) in ethanol (8 mL) was spin-coated at 3000 rpm for 30 s and dried at 110 °C for 10 min. Then, the substrate was annealed at 500 °C for 30 min using a box furnace to form compact TiO_2 (c-TiO_2). To fabricate the AAO on the c-TiO_2 layer, the Al film (thickness of ~270 nm) was thermally evaporated on a 4 × 6.5 cm^2 substrate[18]. Subsequently, anodization of the Al film was performed in an oxalic acid solution (30.12 g of oxalic acid (Sigma–Aldrich) in 800 mL of DI water) by applying a 40-V direct-current voltage using a C cathode. After the anodization procedure, the substrate was rinsed with distilled water. Subsequently, the substrate was dipped in a phosphoric acid solution (20 mL of phosphoric acid (85 wt.% in H_2O, 99.99%, Sigma–Aldrich) in 545 mL of DI water) for 30 min for a widening procedure, followed by rinsing with distilled water. Then, the substrate was post-annealed at 500 °C for 30 min to eliminate the organic residues. After cooling, the AAO substrates were subjected to O_2 plasma treatment for 5 min and left in a dry-air-filled glovebox. Then, a 26 wt.% perovskite precursor solution of MAI (CH_3NH_3I, 99.9%, Dyesol) and lead chloride ($PbCl_2$, 99.999%, Sigma–Aldrich) with a 3:1 molar ratio in a solvent of DMF (anhydrous 99.9%, Sigma–Aldrich) was spin-coated at 3000 rpm for 60 s immediately after 1 min of vacuum-assisted infiltration, followed by annealing on a 105 °C hotplate for 105 min. A solution of 72 mg of 2,2′,7,7′-tetrakis(N,N-di-4-methoxyphenylamino)-9,9′-spirobifluorene (spiro-OMeTAD, 99.9%, Sigma–Aldrich) in 1 mL of chlorobenzene, along with 28.8 µL of 4-tert-butylpyridine and 17.6 µL of a bis(trifluoromethane)-sulfonimide lithium salt solution (520 mg in acetonitrile), was spin-coated at 3000 rpm for 30 s to fabricate the hole-transport layer. For the series-connected PV device with two cells, etched lines 70 µm wide (P1 etching) were formed using a laser scribing system for disconnecting the bottom electrode (µ-LAB, wavelength of 1080 nm, Korthem Science, Korea), under the following conditions: power of 200 µJ, scan speed of 1200 mm/s, and frequency of 50 kHz. After the P1 etching for the full device, a 20-nm MoO_x buffer layer was thermally evaporated onto the spiro-OMeTAD layer. Subsequently, for forming the interconnection region between the top and bottom electrodes of neighboring cells, P2 etching was performed under the following conditions: a 180-µm line width, 65-µJ laser power, and 0.04-mm line interval. After the 250-nm-thick indium-doped tin oxide (ITO) top electrode was sputtered (1.2 mTorr of Ar, 30 W, 10000 s), P3 etching was performed for disconnecting the top electrode.

PEC Performance Evaluation of Sb_2Se_3 Photocathodes

PEC measurements of the Sb_2Se_3 photocathodes were performed for a conventional three-electrode configuration using a potentiostat (SI 1287, Solartron, Leicester, UK) with an Ag/AgCl/KCl (saturated) electrode and coiled Pt wire as the reference and counter electrodes, respectively. The photocathodes were immersed in an H_2SO_4 solution (pH of 1), and the light source was simulated 1-sun illumination (air mass (AM) 1.5G, Newport Corporation). A monocrystalline Si standard reference cell (Newport Corporation) was used for calibration of the light intensity to 1 sun. The scan rate for the J–V curves was 20 mV s^{-1}. To convert the potential, the following equation was employed. $E_{RHE} = E_{Ag/AgCl} + 0.059\ pH + 0.197$. An electrochemical workstation (Zennium, Zahner, Germany) in conjunction with a monochromatic light source (TLS03, Zahner, Germany) was used to measure the IPCE. A gas chromatograph (6500GC system, YL Instruments, Korea) was employed for calculating the Faradaic efficiency via gas-product analysis.

Characterizations of Perovskite Cell

The transmittance was determined using an integrating sphere (ARMN-735, Jasco, Japan) combined with UV–visible spectroscopy (V-670, Jasco, Japan). The PCE was measured under 100-mW/cm^2 (1-sun) illumination from an AM 1.5 solar simulator (Sol3A Class AAA, Oriel Instrument, Irvine, USA) using a Xe arc lamp. The active area was defined by using a metal mask with a 4 mm × 5 mm (0.2 cm^2) hole. The scan rate was 200 mV s^{-1}. To measure the EQE, an electrochemical workstation (Zennium, Zahner, Germany) was used in conjunction with a monochromatic light source (TLS03, Zahner, Germany).

Tandem Cell Assembly and Overall Water Splitting

The active area of the perovskite cells was defined by a 0.2-cm^2 metal mask. Each device was placed in a custom-made Teflon sample holder. The DSA was positioned at the back, approximately 2 cm from the photocathode. The electrochemical cell was filled with an H_2SO_4 solution, and an Ar flow was bubbled through the cell. A perovskite PV cell was placed in front of the electrochemical cell. The PV cell was illuminated with 1-sun light (AM 1.5G, Newport Corporation), and the transmitted light reached the Sb_2Se_3 photocathode through the electrolyte. The PV FTO bottom contact (electron collector) was connected to the photocathode by a Cu wire, while the top contact of the PV cell (ITO hole collector) was connected (through a potentiostat in the two-electrode configuration) to the DSA. A Si diode (Newport Corporation) was used for calibrating the light intensity so that the PV was located at the position corresponding to the 1-sun level. The

scan rate for the J–V curves was 20 mV s^{-1}. The perovskite cell was located in front of the photocathode during the IPCE measurement of the Sb_2Se_3 electrode in a tandem configuration, and a potential of 0 V_{RHE} was applied to the photocathode.

Conclusions

We fabricated efficient and stable PV-PEC tandem devices comprising low-cost Sb_2Se_3 photocathodes and semitransparent perovskite PVs. To accomplish this, we leveraged the state-of-the-art Sb_2Se_3 photocathode enabled by proper junction layers. By inserting a thin SnO_2 layer on top of the TiO_2/CdS/Sb_2Se_3 junction, we enhanced the light-harvesting capability of the Sb_2Se_3 photocathode, particularly for long-wavelength photons (>600 nm). The enhanced light harvesting and the resulting high photocurrent were enabled by the improved charge separation due to selective extraction of the photoexcited electrons by the SnO_2 layer. We found that the maximum η_{STH} of 13% can be achieved by combining the Sb_2Se_3 photocathode with an ideal PV based on the perovskite semiconductor. It was demonstrated that the photocurrent and transmittance of the top PVs could be carefully adjusted while producing sufficient photovoltage to drive the water-splitting reaction by controlling the filling level of the perovskite layer in the AAO scaffold. With careful light management of the top PVs, similar amounts of photons were allocated to the top and bottom electrodes, leading to an η_{STH} of 10%. The high efficiency obtained by the low-cost photocathode represents an important benchmark for practical STH conversion.

Conflicts of interest

The authors declare no competing financial interests.

Acknowledgements

This study was supported by a National Research Foundation (NRF) of Korea grant (no. 2012R1A3A2026417) funded by the Ministry of Science and ICT. This work was also supported by the Technology Innovation Program - Alchemist Project (No. 20012315) funded by the Ministry of Trade, Industry & Energy (MOTIE, Korea).

References

1 W. Yang, R. R. Prabhakar, J. Tan, S. D. Tilley, and J. Moon, *Chem. Soc. Rev.*, 2019, **48**, 4979–5015.
2 S. Hu, C. Xiang, S. Haussener, A. D. Berger and N. S. Lewis, *Energy Environ. Sci.*, 2013, **6**, 2984–2993.
3 W. Yang, J. H. Kim, O. S. Hutter, L. J. Phillips, J. Tan, J. Park, H. Lee, J. D. Major, J. S. Lee and J. Moon, *Nat. Commun.*, 2020, **11**, 861.
4 J. H. Kim, J. –W. Jang, Y. H. Jo, F. F. Abdi, Y. H. Lee, R. Krol and J. S. Lee, *Nat. Commun.*, 2016, **7**, 1–9.
5 Y. Pihosh, I. Turkevych, K. Mawatari, J. Uemura, Y. Kazoe, S. Kosar, K. Makita, T. Sugaya, T. Matsui, D. Fujita, M. Tosa, M. Kondo and T. Kitamori, *Sci. Rep.*, 2015, **5**, 11141.
6 J. H. Kim, Y. Jo, J. H. Kim, J. W. Jang, H. J. Kang, Y. H. Lee, D. S. Kim, Y. Jun and J. S. Lee, *ACS Nano*, 2015, **9**, 11820–11829.
7 J. H. Kim, D. Hansora, P. Sharma, J. W. Jang and J. S. Lee, *Chem. Soc. Rev.*, 2019, **48**, 1908–1971.
8 J. Luo, Z. Li, S. Nishiwaki, M. Schreier, M. T. Mayer, P. Cendula, Y. H. Lee, K. Fu, A. Cao, M. K. Nazeeruddin, Y. E. Romanyuk, S. Buecheler, S. D. Tilley, L. H. Wong, A. N. Tiwari and M. Gratzel, *Adv. Energy Mater.*, 2015, **5**, 1501520.
9 B. Koo, D. Kim, P. Boonmongkolras, S. R. Pae, S. Byun, J. Kim, J. H. Lee, D. H. Kim, S. Kim, B. T. Ahn, S. –W. Nam and B. Shin, *ACS Appl. Energy Mater.*, 2020, **3**, 2296–2303.
10 J. Kim, W. Yang, Y. Oh, H. Lee, S. Lee, H. Shin, J. Kim and J. Moon, *J. Mater. Chem. A*, 2017, **5**, 2180–2187.
11 W. Yang, J. Ahn, Y. Oh, J. Tan, H. Lee, J. Park, H. –C. Kwon, J. Kim, W. Jo, J. Kim and J. Moon, *Adv. Energy Mater.*, 2018, **8**, 1702888.
12 J. Tan, W. Yang, Y. Oh, H. Lee, J. Park, R. Boppella, J. Kim and J. Moon, *Adv. Energy Mater.*, 2019, **9**, 1900179.
13 H. Lee, W. Yang, J. Tan, Y. Oh, J. Park and J. Moon, *ACS Energy Lett.*, 2019, **4**, 995–1003.
14 J. Park, W. Yang, J. Tan, H. Lee, J. W. Yun, S. G. Shim, Y. S. Park and J. Moon, *ACS Energy Lett.*, 2020, **5**, 136–145.
15 W. Yang and J. Moon, *J. Mater. Chem. A*, 2019, **7**, 20467–20477.
16 R. R. Prabhakar, W. Septina, S. Siol, T. Moehl, R. Wick-Joliat and S. D. Tilley, *J. Mater. Chem. A*, 2017, **5**, 23139–23145.
17 H. –C. Kwon, A. Kim, H. Lee, D. Lee, S. Jeong and J. Moon, *Adv. Energy Mater.*, 2016, **6**, 1–11.
18 H. C. Kwon, S. Ma, S. –C. Yun, G. Jang, H. Yang and J. Moon, *J. Mater. Chem. A*, 2020, **8**, 1457–1468.
19 B. Seger, S. D. Tilley, T. Pederson, P. C. K. Vesborg, O. Hansen, M. Grätzel and I. Chorkendorff, *J. Mater. Chem. A.*, 2013, **1**, 15089–15094.
20 J. Azevedo, S. D. Tilley, M. Schreier, M. Stefik, C. Sousa, J. P. Araujo, A. Mendes, M. Gratzel and M. T., *Nano Energy*, 2016, **24**, 10–16.
21 J. Park, W. Yang, Y. Oh, J. Tan, H. Lee, R. Bopella and J. Moon *ACS Energy Lett.*, 2019, **4**, 517–526.
22 Y. X. Yu, L. Pan, M. –K. Son, M. T. Mayer, W. –D. Zhang, A. Hagfeldt, J. Luo and M. Gratzel, *ACS Energy Lett.*, 2018, **3**, 760–766.
23 W. Yang, Y. Oh, J. Kim, M. J. Jeong, J. H. Park and J. Moon, *ACS Energy Lett.*, 2016, **1**, 1127–1136.
24 Y. Zhou, D. Shin, E. Ngaboyamahina, Q. Han, C. B. Parker, D. B. Mitzi and J. T. Glass, *ACS Energy Lett.*, 2018, **3**, 177–183.
25 K. Wang, D. Huang, L. Yu, K. Feng, L. Li, T. Harada, S. Ikeda and F. Jiang, *ACS Catal.*, 2019, **9**, 3090–3097.
26 S. Manzoor, J. Hausele, K. A. Bush, A. F. Palmstrom, J. C. Iii, Z. J. Yu, S. F. Bent, M. D. Mcgehee and Z. C. Holman, *Opt. Express*, 2018, **26**, 27441.
27 H. C. Kwon and J. Moon, *Curr. Opin. Electrochem.*, 2018, **11**, 114–121.
28 P. Dias, M. Schreier, S. D. Tilley, J. Luo, J. Azevedo, L. Andrade, D. Bi, A. Hagfeldt, A. Mendes, M. Gratzel and M. T. Mayer, *Adv. Energy Mater.*, **2015**, 5, 1–9.
29 J. Brillet, J. –H. Yum, M. Cornuz, T. Hisatomi, R. Solarska, J. Augustynski, M. Graetzel and K. Sivula, *Nat. Photonics*, **2012**, 6, 824–828.
30 F. F. Abdi, L. Han, A. H.M. Smets, M. Zeman, B. Dam and R. Krol, *Nat. Commun.*, 2013, **4**, 1–7.
31 L. Han, F. F. Abdi, R. Krol, R. Liu, Z. Huang, H. –J. Lewerenz, B. Dam, M. Zeman and A. H. M. Smets, *ChemSusChem*, 2014, **7**, 2832–2838.
32 Gurudayal, D. Sabba, M. H. Kumar, L. H. Wong, J. Barber, M. Gratzel and N. Mathews, *Nano Lett.*, 2015, **15**, 3833–3839.
33 Y. Qiu, W. Liu, W. Chen, G. Zhou, P. –C. Hsu, R. Zhang, Z. Liang, S. Fan, Y. Zhang and Y. Cui, *Sci. Adv.*, 2016, **2**, e1501764.

34 Y. W. Lee, P. Boonmongkolras, E. J. Son, J. Kim, S. H. Lee, S. K. Kuk, J. W. Ko, B. Shin and C. B. Park, *Nat. Commun.*, 2018, **9**, 4208.
35 V. Andrei, R. L. Z. Hoye, M. Crespo-Quesada, M. Bajada, S. Ahmad, M. D. Volder, R. Friend and E. Reisner, *Adv. Energy Mater.*, 2018, **8**, 1801403.
36 X. Li, M. Jia, Y. Lu, N. Li, Y. –Z. Zheng, X. Tao and M. Huang, *Electrochim. Acta,* 2020, **330**, 135183.
37 R. Fan, S. Cheng, G. Huang, Y. Wang, Y. Zhang, S. Vanka, G. A. Botton, Z. Mi and M. Shen, *J. Mater. Chem. A*, 2019, **7**, 2200–2209.
38 K. Zhang, M. Ma, P. Li, D. H. Wang and J. H. Park, *Adv. Energy Mater.*, 2016, **6**, 1–16.
39 O. S. Hutter, L. J. Phillips, K. Durose and J. D. Major, *Sol. Energy Mater. Sol. Cells*, 2018, **188**, 177–181.